

DME/TACAN Multipath Impact on GNSS L5/E5a Airborne Receivers

Part II: Air-Ground Channel Model and Application

NICOLAS GAULT
ALEXANDRE CHABORY
AXEL GARCIA-PENA
CHRISTOPHE MACABIAU

École Nationale de l'Aviation Civile, Toulouse, France

This article is the second part of a two-part manuscript addressing the DME/TACAN multipath impact on the future airborne GNSS L5/E5a receivers. Part I developed the analytical carrier-to-noise-ratio degradation model due to DME/TACAN considering multipath, in the presence of a temporal blanker. Part II introduces a theoretical hybrid determinist-stochastic wideband Air-Ground geometry-based channel model. The model includes an Okumura-Hata path loss for the illuminated scatterers, an analytical formula for the additional delay generated by the scatterers with respect to the direct signal and the mathematical expression of the scattered power generated by the scatterer. Given the very high number of scatterers to be considered for an Air-Ground scenario, a statistical simplification of the Physical Optics approach is introduced to simplify the derivation of the scattered powers. The propagation channel and the carrier-to-noise-ratio mathematical degradation models are applied to two low-altitude operational hot-spots, JALTO (Pennsylvania, United-States) and TIXAK (Frankfurt, Germany). It is shown that only a few scatterers generate a scattered power above the blanking threshold and that the additional carrier-to-noise-ratio degradation generated by the DME/TACAN multipath only is less than 0.33 dB.

I. INTRODUCTION

The nominal processing of Global Navigation Satellite System (GNSS) received signals can be affected by noise as well as received additive signals such as multipath (MP) and Radio Frequency Interference (RFI) [1]. GNSS L5/E5a interference environment is predominantly dominated by pulsed interferences such as DME/TACAN and JTIDS/MIDS [2]. In the context of civil aviation, the RFI impact on a GNSS receiver is internationally standardized by the International Civil Aviation Organization (ICAO), in the United States by

the Radio Technical Commission for Aeronautics (RTCA) and in Europe by the European Organization for Civil Aviation Equipment (EUROCAE). In these standards, the RFI impact is usually modelled as the C/N_0 degradation observed at the receiver antenna port when considering ideal the receiver Radio Frequency Front End (RFFE) elements (Low Noise Amplifier (LNA), Mixer, Radio Frequency (RF) and Intermediate Frequency (IF) filters, Automatic Gain Control/Analog to Digital Converter (ADC/AGC)) [1], [2],[3].

To mitigate the impact of the pulsed RFI observed in the L5/E5a band, a temporal blanker in the airborne GNSS receiver RFFE block is assumed to be implemented by the civil aviation standards in Dual-Frequency Multi-Constellation (DFMC) GNSS receivers [1],[4]. The role of the blanker is to set the received signal samples to zero when their instantaneous power envelope exceeds a predefined threshold. The percentage of samples set to zero by the blanker is referred to as the blanking duty-cycle (bdc) and the below-blanker interfering signal-to-noise-ratio as R_I . From R_I and bdc , the value of the C/N_0 degradation solely due to pulsed interferences is derived.

However, no previous work considered any multipath effect which is especially important since echoed pulses could impact the GNSS receiver in the same manner as the direct pulse. In Part I of this two-part manuscript [5], the mathematical expressions for R_I and bdc were updated to provide a statistical average of the C/N_0 degradation including the DME/TACAN MP for a given aircraft position. The application of the new C/N_0 degradation model requires the precise knowledge of the additional delays of the echoed pulses with respect to the direct pulse as well as their scattered powers at the aircraft's antenna port. Therefore, an air-to-ground (AG) aeronautical propagation channel model specifically suitable for RFI analysis is needed.

In the scenarios analyzed in this study, DME/TACAN beacons situated on the ground transmit a signal close to the L5 frequency (1176.45 MHz) to an aircraft at an altitude from a few hundred of meters to kilometers and a slant range of a few tens of kilometers. For this reason, the analyzed scenes are very large and the additional delays of the received echoed pulses are expected to be much greater than the DME/TACAN pulse duration ($\approx 10 \mu s$). Therefore, the required AG channel model must absolutely be wideband, i.e., account for these delays. Furthermore, millions of scatterers in the Radio Line Of Sight (RLOS) of the aircraft are potentially generating MP. Consequently, the targeted propagation channel model must be able to cope with a very high number of scatterers without being too computationally expensive while still being representative from an RFI point of view.

One way forward to derive the required propagation channel model is to analyze the research conducted in the literature for applications with similar constraints such as Unmanned Aerial Vehicles (UAVs). Indeed, with the recent interest UAVs from both scientific and industry communities, many AG channel models have been developed in the literature and are extensively summarized in numerous surveys [6], [7], [8], [9]. Given the relatively low altitude of the aircraft or the

UAV and the relatively high emitting antenna height, the AG propagation channel presents similar technical challenges to the ones found in the target channel such as accounting for scattering, reflection, diffraction and shadowing from millions of scatterers, reflectors, trees and forests in potentially very complex environments.

To cope with these challenges, the most commonly found solutions in the literature are the measurement-based AG channel models. For example, widely cited papers from Matolak *et al.* introduce a propagation channel model based on an extensive measurement campaign conducted in four different environments across the United-States: over-water, hilly/mountainous, urban and suburban [10],[11],[12]. A more recent study from Schneckenburger *et al.* present an aeronautical AG Geometrically Based Stochastic Channel Model (GBSCM) based on two L-band (1 GHz – 2 GHz) flight trials conducted in Germany validated against measurements [13],[14]. The so-called statistical theoretical AG models, generally offering the advantage of being both simple and computationally efficient, are dependent on the estimation of their statistical parameters, e.g. the Rice factor, which have to be extracted from measurements [15],[16],[17],[18].

However, even if measurement campaigns always provide highly valuable insights into both the channel and the environment (number of MP, position of the scatterers by means of super-resolution algorithms [19], etc.), they are always extremely expensive and time-consuming and thus limited in terms of number of investigated locations [10],[20]. Furthermore, the applicability of these measurement-based AG channel models to locations where measurements campaigns have not been conducted still needs to be demonstrated. For these reasons, an alternative AG channel model not based on measurement but still coping with the presence of a very high number of scatterers is proposed in this analysis.

Not measurement-based channel models are deterministic or hybrid deterministic-stochastic (HDS) theoretical channel models. Deterministic or HDS theoretical channel models aim at reproducing the physical electromagnetic (EM) wave propagation in a given environment (determinist or statistical). Depending on the targeted accuracy, the wave interactions are usually modelled by means of full-wave (or exact) methods such as the Method of Moment (MoM) or by asymptotic methods such as the Uniform Theory of Diffraction (UTD) or Physical Optics (PO). However, to the best knowledge of the authors, there is no deterministic or hybrid deterministic-statistical theoretical AG channel model available in the literature.

The deterministic or HDS theoretical channel models most analogous to AG models are the Land-Mobile-Satellite (LMS) models specifically designed for GNSS applications. LMS models designed for GNSS applications are analogous to the AG models since they investigate a ground/sky link in the L-band and are wideband-designed channel models since the time of arrival of MP must be known to predict the pseudorange measurement error in the estimation of the Position, Velocity and Time (PVT). One example is the propagation channel

model developed by Chen *and al.*, a fully deterministic theoretical channel model based on a PO asymptotic approach to investigate the effect of GNSS MP on the airborne GNSS receiver in an airport environment [21]. The PO approach is numerically validated against MoM and the overall channel performance is compared against measurements. Another notable example is the Simplified CHannel for Urban Navigation (SCHUN) model proposed by Ait-Ighil [22]. In this model the effect of GNSS MP on GNSS receivers in a urban environment is investigated using a PO approach in combination with a simplified stochastic urban environment [23]. The SCHUN propagation channel model elements and assumptions are also numerically validated against MoM and confronted with measurements.

However, the LMS models only investigate a local environment around the receiver where only a few scatterers are generating MP, given the low receiving antenna height. Additionally, the illumination of scatterers differs between LMS and AG scenarios due to the higher elevation angles of the received signals in LMS. Consequently, the set of assumptions considered in the LMS models must be adapted for the AG model. Above all, , for AG channels the simulation of the (EM) interactions must be simplified to consider the very high number of scatterers potentially generating MP across very large scenes.

Therefore, the objective of this paper is to propose a theoretical hybrid deterministic-stochastic wideband AG Geometrically Based Channel Model (GBCM) specially suitable for the AG environment. The objective of the proposed AG channel is to provide the scattered powers and the additional delays generated by the scatterers for a given aircraft position to obtain the statistical average of the C/N_0 degradation as developed in [5]. However, acknowledge that the proposed AG channel is not restricted to the interference analysis: all the mathematical models (except for the phase) needed to generate the Channel Impulse Response (CIR) time series for a complete aircraft trajectory are provided in the article. Furthermore, the proposed AG model is not limited to the DME/TACAN system analysis: the model could be easily reused for any other AG system operating in the L5 band, such as L-band digital aeronautical communication (LDACS), Digital Video Broadcasting–Terrestrial (DBV-T), Digital Audio Broadcasting (DAB), primary or secondary radar etc.

Additionally, the proposed AG channel model and the C/N_0 mathematical degradation model presented in [5] are applied to two low-altitude operational hot-spots to provide a numerical example of the statistical average of the additional C/N_0 degradation generated by the consideration of the DME/TACAN MP. Note that a first version of the proposed AG channel model was previously proposed in [24] by the same authors but has been largely modified and enhanced since. Moreover, the mathematical models used to derive the propagation channel were not detailed.

The article is organized as follows. Section II provides a global description of the proposed AG channel model with the introduction of the CIR. Section III introduces the

determination of the CIR parameters. Given the high number of scatterers considered, section IV proposes a statistical simplification of the classical PO approach to reduce the overall computation time. Section V summarizes the general methodology to obtain the statistical average of the C/N_0 degradation in presence of MP, utilizing the proposed AG channel model and the analytical formulas for R_I and bdc presented in Part I [5]. Section VI is dedicated to the presentation of two numerical applications of the model at two low altitude operational hot-spots: JALTO (Philadelphia, USA) and TIXAK (Frankfurt, Germany). Section VII concludes the analysis.

II. PROPAGATION CHANNEL MODEL DESCRIPTION

In this section, the proposed AG channel model with its CIR are described. The proposed AG channel model investigates a single DME/TACAN beacon and aircraft configuration. Fig. 1 shows an illustration of the proposed AG propagation channel model.

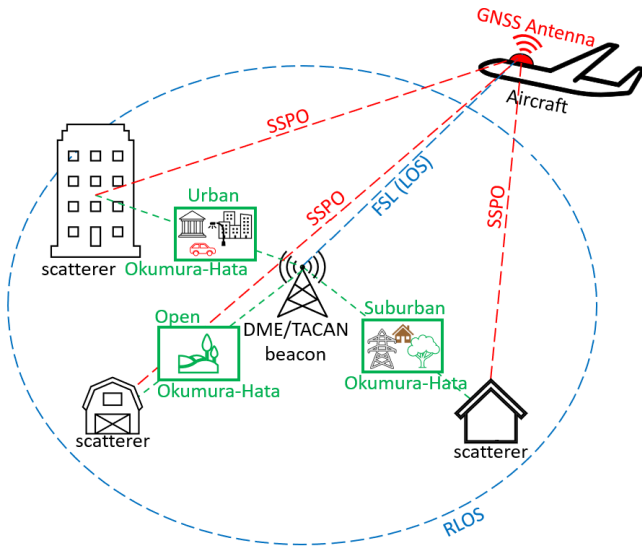


Fig. 1. Illustration of the proposed AG propagation channel model.

In Fig. 1, the DME/TACAN beacon transmits a signal to the aircraft airborne DME/TACAN transponder. Since the signal is emitted in the L5 band, the DFMC receiver, situated on the top of the aircraft, also receives the signal and is therefore victim of RFI. The direct path between the beacon and the aircraft is denoted as the Line of Sight (LOS) signal. The LOS signal power is assumed to follow Free Space Loss (FSL).

Moreover, other elements situated in the RLOS of the DME/TACAN beacon potentially scatter the DME/TACAN signal, producing echoed pulses arriving at the DFMC GNSS receiver antenna with an additional delay τ_i with respect to the LOS. The elements scattering the signal are referred as scatterers in this article. The illumination of the scatterers is

assumed to follow a Okumura-Hata statistical model [25] presented in Section III and the power scattered by the scatterers at the receiver antenna output is computed by means of a Statistical Simplification of the classical PO approach (SSPO) introduced in Section IV. For these reasons, the proposed channel model can be considered as an hybrid deterministic-stochastic model. Furthermore, the scattered powers and additional delays depend on the scatterer positions (among a few other scatterers inputs) and thus the proposed AG channel model is a GBCM.

The aircraft on which the DFMC GNSS receiver antenna is placed is moving with time. Along its trajectory, the channel is modelled by means of the time-variant CIR $h_{CIR}(t, \tau)$ which can be expressed as, for the DME/TACAN beacon m [26],

$$h_{CIR}^m(t, \tau) = \sum_{i=0}^{N_m(t)} \alpha_i(t) e^{j\phi_i(t)} \delta(\tau - \tau_i(t)), \quad (1)$$

where N_m is the number of MP generated by the DME/TACAN beacon m , and $(\alpha_i, \phi_i, \tau_i)$ are the MP amplitude, phase and additional delay, respectively. The index $i = 0$ is associated with the LOS signal. The variable τ is used to convolute the time-variant CIR with the DME/TACAN beacon m transmitted signal, $s_m(t)$, to obtain the received signal $r_m(t)$ at the GNSS receiver antenna port. When multiple DME/TACAN beacons are visible from the aircraft, the received signal $r_m(t)$ is derived for all the beacons and the total received signal is retrieved by summing all $r_m(t)$.

Three important remarks must be highlighted regarding equation (1):

1. The objective of this analysis is to provide a statistical average of the C/N_0 degradation at two operational hot-spots: JALTO and TIXAK. Therefore, the aircraft trajectories investigated in this study are only single waypoints. For single waypoint trajectories, the carrier phases of two MPs are assumed to be independent and uniform on $[0, 2\pi]$ and thus no time evolution of the phase is provided in this work since it is not necessary. For a discussion of the time evolution of the carrier phase value, the reader is referred to [5].
2. The C/N_0 degradation model accounting for multipath as developed in [5] requires the scattered power P_i generated by the scatterers and not the MP amplitude α_i . Therefore in this article, only the analytical expression of P_i is provided. The relationship between P_i and α_i is given by $\alpha_i = \sqrt{P_i}$.
3. To prevent the notations from becoming too cumbersome for the determination of the analytical expression of N_m , P and τ , the sub-index i , referring to a single scatterer, is no longer used for the rest of the article.

To summarize, the objective of the proposed channel model is to determine the number of scatterers generating MP N_m (see section III.A), their additional delay τ (section III.C) and scattered power P (section III.F for the exact expression and section IV for the simplification) for any aircraft position from a few information about the scatterers.

III. DETERMINATION OF THE CHANNEL IMPULSE RESPONSE PARAMETERS

In this section, the number of illuminated scatterers N , the analytical expression of the additional delay τ and the scattered power P of the scatterers at a given aircraft position are provided. Since P relies on the scattered electric field \mathbf{E}_s at the DMFC receiving antenna output, the analytical expression of \mathbf{E}_s is also introduced. Given the complexity of the scene (dimension of the scene, number and diversity of the scatterers etc.), the set of simplifications and assumptions to reach a trade-off between simplicity and realism from an RFI point of view is also presented.

The section is organized as follows. Section III.A presents the assumptions concerning the number N of scatterers generating MP. Section III.B introduces the illumination model of the considered scatterers. Section III.C provides the set of assumptions and the analytical expression of the additional delay τ . Section III.D describes the assumptions for the MP scattered power P . Section III.E is dedicated to derivation of the analytical expression of the scattered electric field \mathbf{E}_s in the case of a smooth and heterogeneous scatterer based using PO. The electric field \mathbf{E}_s is used to derive the scattered power P in Section III.F. Section III.G concludes by discussing the limitation of the considered approach.

A. Determination of the Illuminated Scatterers N_m

In this section, the assumptions used for the determination of the illuminated scatterers N_m , namely the RLOS and the building facades, are presented.

RLOS: Only the obstacles that are in the RLOS of the DME/TACAN beacons are kept as potential candidates to scatter the direct signal. Using an effective earth radius of $4/3R_T$, where R_T is the actual earth radius, the RLOS for a given beacon is formulated as [27]

$$RLOS = \sqrt{(4/3 R_T + H_{DME})^2 - (4/3 R_T)^2} + \sqrt{(4/3 R_T + H)^2 - (4/3 R_T)^2}, \quad (2)$$

where H_{DME} is the height of the DME/TACAN beacon antenna and H is the height of the scatterer. As an example, with a height above ground of the DME/TACAN beacon antenna H_{DME} of 10 m and a scatterer height H of 10 m, the RLOS is approximately 25 km.

Building Facade: Within such a large scene in densely populated areas, millions of scatterers of various sorts such as buildings, trees, cars etc. are potentially generating MP. Since buildings facades are assumed to be the elements generating the most powerful MP, only the building facades are considered as scatterers in this analysis. Note that the effect of other elements is considered in the building illumination (section III.B). Therefore, the number of scatterers N_m is obtained by counting all the building facades in the RLOSs of the DME/TACAN beacon.

B. Scatterers illumination

In this section, the assumptions concerning the illumination of the scatterers and the determination of the Okumura-Hata environment are presented.

Scatterers illumination: The considered scatterers (see section III.A) are illuminated considering an Okumura-Hata model [25]. The Okumura-Hata model aims at predicting path-loss due to fading and shadowing provoked by the overall environments (buildings, trees, cars, ground relief, electric pylons etc.) in urban, suburban and open environments in the 150-1500 MHz frequency band. For the urban case, the path-loss $L_H^{u,dB}$ in dB is expressed as

$$L_H^{u,dB} = 69.55 + 26.16 \log(f) - 13.82 \log(H_{DME}) - C_H + [44.9 - 6.55 \log(H_{DME})] \log(R_1), \quad (3)$$

where

$$C_H = 3.2(\log(11.75H))^2 - 4.97, \quad (4)$$

f is the carrier frequency in MHz and R_1 is the distance between the DME/TACAN beacon and the scatterer. For the suburban environments, the path-loss $L_H^{su,dB}$ in dB is given by

$$L_H^{su,dB} = L_u - 2 \left(\log\left(\frac{f}{28}\right) \right)^2 - 5.4, \quad (5)$$

and for the open environments, the path-loss $L_H^{o,dB}$ in dB is

$$L_H^{o,dB} = L_H^{u,dB} - 4.78(\log(f))^2 + 18.33 \log(f) - 40.94. \quad (6)$$

Determination of the Okumura-Hata environment: When no other scatterer exists along the direct path from the beacon to the considered scatterer, the scatterer is considered to be in LOS, and consequently in an open environment in this analysis and (6) applies. The scatterers having a direct path obstructed by other scatterers are either considered to be in a urban or a suburban environment and either (4) or (5) applies, depending on the density of buildings at the DME/TACAN beacon localization. Fig. 2 provides an example of the Okumura-Hata environment determination where the LOS green scatterer obstructs the red scatterer.

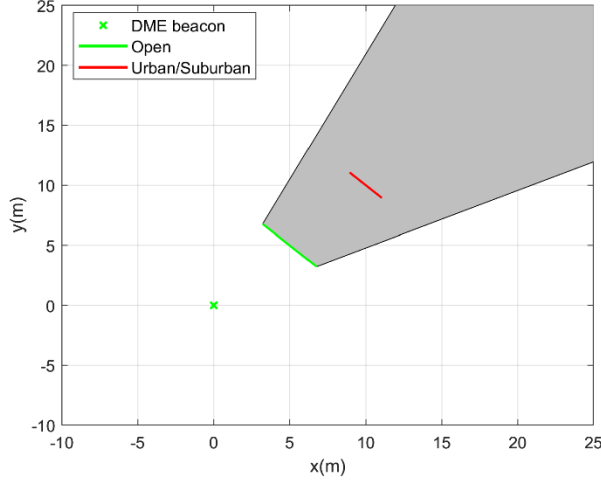


Fig. 2. Example of the proposed Okumura-Hata environment determination.

C. Analytical Expression of The Multipath Additional Delay τ

In this subsection, the assumptions used for the additional delay computation, namely the first-order interaction and the earth flat without bending, are first presented. Second, considering the assumptions the analytical expression of the additional delay τ is provided.

First-order Interaction: To simplify the analysis, the scatterers can only scatter the field coming from the DME/TACAN beacon's antenna and not from any other scatterer.

Flat Earth And Without Refraction: To simplify the model, the Earth is considered as flat for the additional delay analysis. Furthermore, all the paths are considered as straight lines, meaning that the tropospheric refraction effect is not considered.

Considering the previous assumptions, the formula of the additional delay τ_i of the echoes with respect to the LOS signal is given by

$$\tau = \frac{R_1 + R_2 - D}{c}, \quad (7)$$

where R_2 is the distance between the obstacle and the aircraft, D is the distance between the DME/TACAN beacon and the aircraft (direct path) and c is the free-space speed of light.

D. Assumption For The Multipath Scattered Power P

In this section, the assumptions used for the scattered power P , namely the PO approach, the far-field propagation model and the scatterers composition and shape, are provided.

PO approach: PO is assumed for modelling the EM interactions. Instead of solving rigorously the Maxwell's equation as it is done for the full-wave methods (Method of Moments, Finite Difference in Time Domain etc.), PO is an

asymptotic method where the Maxwell equations are solved by means of the determination of the equivalent currents and the use of the Stratton-Chu integrals [28]. Asymptotic methods are much faster and cost-efficient than the Full-Wave methods and are thus more suitable for the very large number of scatterers considered in this study. Note that PO is only valid for scatterers larger than three wavelengths (≈ 75 cm) which is always true for buildings. PO is also validated against measurements [29].

Far-field Propagation Model: The scattered power P derivation is made assuming a far-field propagation model, meaning that the scatterer must be in the far-field of the DME/TACAN beacon antenna and that the aircraft must be in the far-field of the obstacle. Indeed, the computation of the Stratton-Chu integrals is quicker in that case while still being valid [30]. An object A is in the far-field of an object B if

$$R \geq \frac{2L^2}{\lambda}, \quad (8)$$

where R is the distance between A and B , L is the largest dimension of object A and λ is the wavelength associated with the DME/TACAN carrier frequency.

In the case where the scatterer is too large to comply with this condition, the scatterer is divided in smaller elements such that every elements respects the far-field condition. Fig. 3 provides an example of that process, where the initial obstacle is divided three times.

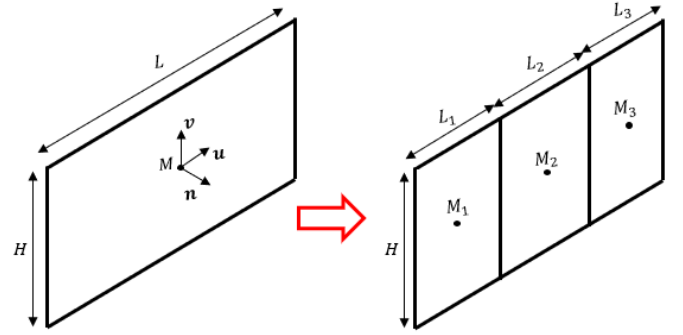


Fig. 3. Example of the proposed methodology to ensure that the far-field condition is always respected.

In Fig. 3, L is the length of the scatterer, M is the scatterer center, \mathbf{n} is the outgoing normal vector to the obstacle and \mathbf{u} and \mathbf{v} are the unit vectors completing the orthonormal basis.

Scatterer Composition and Shape: To simplify the analysis, the building facades are assumed to be composed by one dominant material among four different available materials: metal, concrete, brick, and wood. In addition to the dominant material, windows composed of glass are also introduced in the facades. The materials are modeled as slabs characterized by a thickness t_h and a permittivity ϵ_r . The values of t_h and ϵ_r for the 5 materials are provided in the two

first columns of Table I. Furthermore, the building facades are considered perfectly rectangular in the analysis.

TABLE I
Permittivity ϵ_r , thickness t_h and $|h_v(0,0)|$ for the 5 materials

Material	ϵ_r	t_h (cm)	$ h_v(0,0) $
Metal	-	30	0.65
Concrete	6.5-j0.4	30	0.74
Brick	3.75-j0.68	30	0.76
Wood	1.42-j0.02	30	1.44
Glass	5-j0.025	0.5	-

E. Derivation of The Scattered Field \mathbf{E}_s In The Case of a Smooth and Heterogeneous Scatterer

The derivation of the scattered field \mathbf{E}_s at the aircraft GNSS antenna electrical phase center in the case of a smooth and heterogeneous is necessary in order to obtain the MP scatterer power P . In this article, a scatterer is said smooth is no small details are represented and heterogeneous if it is composed of a combination of one material (metal, brick, concrete or wood) and at least one window (composed of glass). Fig. 4 shows an example of a rectangular smooth and heterogeneous building facade from the ENAC campus.

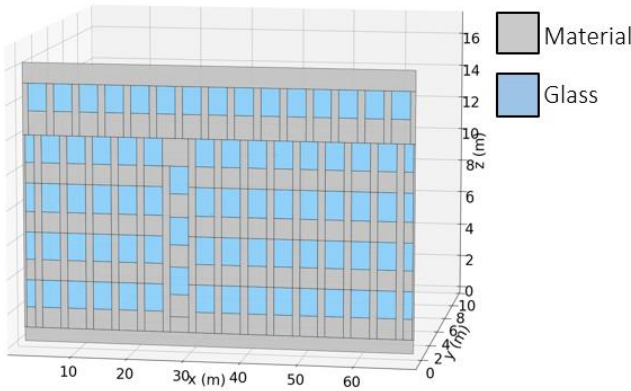


Fig. 4. Example of a rectangular smooth and heterogeneous building facade from the ENAC campus building

Scene presentation and notation: The DME/TACAN beacon antenna electrical phase center (represented by A), scatterer center (M) and the aircraft GNSS antenna electrical phase center (represented by B) scene are presented in Fig. 5.

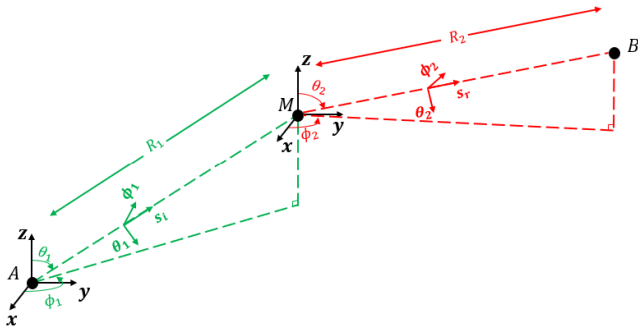


Fig. 5. Representation of the DME-Scatterer-Aircraft scene

In Fig. 5, \mathbf{s}_i and \mathbf{s}_r are the unit vector representing the direction of incidence and observation, respectively,

$$\begin{aligned} \mathbf{s}_i &= \frac{\mathbf{AM}}{R_1} \\ \mathbf{s}_r &= \frac{\mathbf{MB}}{R_2}, \end{aligned} \quad (9)$$

(x, y, z) is the East-North-Up (ENU) frame centered in A , $(\mathbf{s}_i, \theta_1, \phi_1)$ and $(\mathbf{s}_r, \theta_r, \phi_r)$ are the spherical incident and reflected frame, respectively. Furthermore, $\theta_1, \phi_1, \theta_2$ and ϕ_2 are the spherical-coordinate angles for the direction of incidence and observation, respectively.

Derivation of the Scattered Field \mathbf{E}_s : For the smooth and heterogeneous scatterers, the PO approach implies to mesh the scatterer in a number Q of elements such that each element is smooth and homogeneous. In this article, an obstacle is said homogenous if it is composed of only one material (here metal, concrete, brick, wood or glass). After meshing, the scattered field \mathbf{E}_s is given by

$$\mathbf{E}_s = \sum_{q=1}^Q \mathbf{E}_s^{sh,q}, \quad (10)$$

where $\mathbf{E}_s^{sh,q}$ is the scattered field of each smooth and homogeneous elements q .

The scattered field $\mathbf{E}_s^{sh,q}$ for a smooth and homogeneous element is derived in the following. Note that the upper-index q is no longer used in the derivation to prevent the notations from becoming overly complex. The scattered field \mathbf{E}_s^{sh} at the aircraft GNSS antenna electrical phase center is derived by means of the far-field formulation of the Stratton-Chu integrals [30]

$$\begin{aligned} \mathbf{E}_s^{sh} = j \frac{k_0}{4\pi} \frac{e^{-jk_0 R_2}}{R_2} \left\{ \zeta_0 \mathbf{s}_r \times \left[\mathbf{s}_r \times \iint_S \mathbf{J}_e(\mathbf{M}') e^{jk_0 \mathbf{s}_r \cdot \mathbf{r}'} dS(\mathbf{M}') \right] \right. \\ \left. + \mathbf{s}_r \times \iint_S \mathbf{J}_m(\mathbf{M}') e^{jk_0 \mathbf{s}_r \cdot \mathbf{r}'} dS(\mathbf{M}') \right\}, \end{aligned} \quad (11)$$

where $k_0 = \frac{2\pi}{\lambda}$ is the wave number, ζ_0 is the free-space impedance, S is the surface of the scatterer, \mathbf{M}' is a point of the obstacle, $\mathbf{r}' = \mathbf{MM}'$ is the vector from the center of the obstacle M to the point \mathbf{M}' , $\mathbf{J}_e(\mathbf{M}')$ and $\mathbf{J}_m(\mathbf{M}')$ are the electric and the magnetic equivalent currents generated at the point \mathbf{M}' , respectively. In the framework of PO, $\mathbf{J}_e(\mathbf{M}')$ and $\mathbf{J}_m(\mathbf{M}')$ are expressed as

$$\begin{aligned} \mathbf{J}_e(\mathbf{M}') &= \frac{1}{\zeta_0} (\mathbf{n} \times (\mathbf{s}_i \times \mathbf{E}_i(\mathbf{M}') + \mathbf{n} \times \mathbf{s}_i \times \mathbf{E}_i(\mathbf{M}')) \\ \mathbf{J}_m(\mathbf{M}') &= -\mathbf{n} \times \mathbf{E}_i(\mathbf{M}') - \mathbf{n} \times \mathbf{R} \mathbf{E}_i(\mathbf{M}'). \end{aligned} \quad (12)$$

Furthermore, \mathbf{s}_r^{sp} , the direction of specular reflection is given by

$$\mathbf{s}_r^{sp} = \mathbf{s}_i + 2 \cos(\theta_i) \mathbf{n}, \quad (13)$$

where θ_i is the angle between \mathbf{s}_i and $-\mathbf{n}$, \mathbf{R} is the Dyadic Fresnel reflection coefficient of the multilayer slab [31] and $\mathbf{E}_i(\mathbf{M}')$ is the vertically polarized electric incident field generated by the DME/TACAN beacon at point \mathbf{M}' . Furthermore, $\mathbf{E}_i(\mathbf{M}')$ is expressed as

$$\mathbf{E}_i(\mathbf{M}') = \sqrt{\frac{8\pi L_H P_{TX} G_{TX}(\theta_1) \zeta_0}{\lambda^2}} e^{-jk_0 R_1} \boldsymbol{\theta}_1 = E_i^0 \boldsymbol{\theta}_1, \quad (14)$$

where L_H is either the linear open, suburban or urban Okumura-Hata path loss as defined in (4),(5) and (6), P_{TX} is the transmitted power of the DME/TACAN beacon and G_{TX} is the gain of DME/TACAN beacon's transmitting antenna.

The incident field is a plane wave on the surface [21]. Therefore, since the scatterer is homogeneous and rectangular, the double integrals in (11) is given by

$$\begin{aligned} \iint_S \mathbf{J}_e(\mathbf{M}') e^{jk_0 \mathbf{s}_r \cdot \mathbf{r}'} dS(\mathbf{M}') &= \mathbf{J}_e(\mathbf{M}) LH \text{sinc}\left(k_0 \frac{UL}{2}\right) \text{sinc}\left(k_0 \frac{VH}{2}\right) \\ \iint_S \mathbf{J}_m(\mathbf{M}') e^{jk_0 \mathbf{s}_r \cdot \mathbf{r}'} dS(\mathbf{M}') &= \mathbf{J}_m(\mathbf{M}) LH \text{sinc}\left(k_0 \frac{UL}{2}\right) \text{sinc}\left(k_0 \frac{VH}{2}\right), \end{aligned} \quad (15)$$

where U and V are expressed as

$$\begin{aligned} U &= (\mathbf{s}_r - \mathbf{s}_i) \cdot \mathbf{u} \\ V &= (\mathbf{s}_r - \mathbf{s}_i) \cdot \mathbf{v}. \end{aligned} \quad (16)$$

Furthermore, combining (12) with (14) yields

$$\begin{aligned} \mathbf{J}_e(\mathbf{M}) &= \frac{E_i^0}{\zeta_0} \mathbf{n} \times [\mathbf{s}_i \times \boldsymbol{\theta}_1 + \mathbf{s}_r^{sp} \times (\mathbf{R}\boldsymbol{\theta}_1)] \\ \mathbf{J}_m(\mathbf{M}) &= -E_i^0 \mathbf{n} \times (\boldsymbol{\theta}_1 + (\mathbf{R}\boldsymbol{\theta}_1)). \end{aligned} \quad (17)$$

Separating the case where the aircraft is in front of the scatterer which can be considered as a reflection and the case where the aircraft is behind the scatterer by means of the principle of equivalence [32], the scattered field \mathbf{E}_s^{sh} can be expressed as

$$\mathbf{E}_s^{sh} = \begin{cases} E_s^0 \boldsymbol{\delta}_b & \text{if } \mathbf{s}_r \cdot \mathbf{n} \leq 0 \\ E_s^0 \boldsymbol{\delta}_r & \text{otherwise,} \end{cases} \quad (18)$$

where

$$E_s^0 = j \frac{k_0 e^{-jk_0(R_1+R_2)}}{R_2} \sqrt{\frac{L_H P_{TX} G_{TX}(\theta_1) \zeta_0}{2\pi\lambda^2}} LH \cdot \text{sinc}(k_0 UL/2) \text{sinc}(k_0 VH/2) \quad (19)$$

and

$$\begin{aligned} \boldsymbol{\delta}_b &= \mathbf{s}_r \times [\mathbf{s}_r \times \mathbf{n} \times \mathbf{s}_i - \mathbf{n}] \times \boldsymbol{\theta}_1 \\ \boldsymbol{\delta}_r &= \mathbf{s}_r \times [\mathbf{s}_r \times \mathbf{n} \times \mathbf{s}_r^{sp} - \mathbf{n}] \times \mathbf{R}\boldsymbol{\theta}_1. \end{aligned} \quad (20)$$

Finally, the scattered field \mathbf{E}_s of a smooth and heterogeneous obstacle is given by

$$\mathbf{E}_s = \begin{cases} \sum_{q=1}^Q E_s^{0,q} \boldsymbol{\delta}_b^q & \text{if } \mathbf{s}_r \cdot \mathbf{n} \leq 0 \\ \sum_{q=1}^Q E_s^{0,q} \boldsymbol{\delta}_r^q & \text{otherwise,} \end{cases} \quad (21)$$

F. Analytical Expression of One Multipath Scattered Power P

From the analytical expression of the scattered field \mathbf{E}_s in case of a smooth and heterogeneous scatterer (21), neglecting the polarization mismatch losses, the scattered power P generated by the scatterer at the airborne antenna output is given by

$$P = \frac{\|\mathbf{E}_s\|^2}{2\zeta_0} S_{eff}^{AC}, \quad (22)$$

where S_{eff}^{AC} is the effective surface of the receiving airborne antenna,

$$S_{eff}^{AC} = \frac{\lambda^2}{4\pi} G_{RX}(\theta_2) \quad (23)$$

and G_{RX} is the received antenna gain assumed to be omnidirectional on the azimuth angle. Therefore,

$$P = \begin{cases} P^0 \|\boldsymbol{\delta}_b\|^2 & \text{if } \mathbf{s}_r \cdot \mathbf{n} \leq 0 \\ P^0 \|\boldsymbol{\delta}_r\|^2 & \text{otherwise,} \end{cases} \quad (24)$$

where P^0 is expressed as

$$P^0 = \frac{L_H P_{TX} G_{TX}(\theta_1) G_{RX}(\theta_2)}{(2R_2\lambda)^2} (LH)^2 \cdot |\text{sinc}(k_0 UL/2)|^2 |\text{sinc}(k_0 VH/2)|^2. \quad (25)$$

G. Discussion on the Proposed Approach

The MP scattered power P has been deterministically determined using PO (21). However, the utilization of this approach presents two major limitations for our AG channel model.

Limitation 1: Equation (22) requires the precise knowledge of all the details of all the obstacles considered for

the study. However, no such knowledge is available for the high number of scatterers used in the analyzed scenarios.

Limitation 2: Even if such knowledge was available, the application of (21) to millions of scatterers would be too computationally expensive.

Therefore, a statistical simplification of the PO approach for the determination of the scattered field is proposed to tackle the two limitations.

IV. STATISTICAL SIMPLIFICATION OF THE PHYSICAL OPTICS APPROACH

The objective of this section is to provide a statistical simplification of PO to overcome both limitations introduced in section III.G. First, the addressing of the limitation 2, introducing the function h , is presented. Second, the handling of the limitation 1, using the ENAC campus building as a reference scatterer, is provided. Third, the analytical expression of the scattered power P using SSPO is introduced, and the necessary inputs needed from the scatterers to apply the proposed AG channel model are presented.

A. Addressing Limitation 2

In this section, Limitation 2 is addressed by introducing a function h and an example of the determination of h is provided for the ENAC campus building.

Limitation 2 concerns the number of operations (computations and meshing) necessary to derive the electric field \mathbf{E}_s in the case of a smooth and heterogenous scatterer expressed in (21). The computational complexity of such method becomes critical as the number of considered scatterers increases.

Therefore, to limit the number of necessary operations to derive \mathbf{E}_s , it is proposed to model the smooth and heterogenous scatterer as a smooth and homogenous scatterer composed of the scatterer dominant material (metal, concrete, brick or wood) excluding the glass windows by means of a simple function $h: \mathbb{R}^2 \rightarrow \mathbb{R}$. The function h is dependant on the dominant material and therefore one function h has to be determined per dominant material. Note that with this modelling, neither the meshing nor the sum are needed anymore since the scatterer is smooth and homogeneous (see equation (18)) and that only the function $|h|$ has to be determined. Using $|h|$, the targeted simplified scattered field is denoted as $\widetilde{\mathbf{E}}_s$. The simplified field $\widetilde{\mathbf{E}}_s$ is expressed as

$$\widetilde{\mathbf{E}}_s = \begin{cases} \widetilde{E}_s^0 \boldsymbol{\delta}_b & \text{if } \mathbf{s}_r \cdot \mathbf{n} \leq 0 \\ \widetilde{E}_s^0 \boldsymbol{\delta}_r & \text{otherwise,} \end{cases} \quad (26)$$

with

$$\widetilde{E}_s^0 = j \frac{k_0 e^{-jk_0(R_1+R_2)}}{R_1 R_2} \sqrt{\frac{P_{TX} G_{TX}(\theta_1) \zeta_0}{32\pi^3}} LH \cdot h\left(k_0 \frac{UL}{2}, k_0 \frac{VH}{2}\right). \quad (27)$$

Since P relies on the Euclidean norm of \mathbf{E}_s (see equation (22)), only the absolute value of $|h|$ is needed to determine \widetilde{E}_s^0 . For a scatterer, a function $|h|$ can be numerically determined by means of simulations knowing the exact composition of the scatterer equalizing (26) to (20). Denoting $a = k_0 \frac{UL}{2}$ and $b = k_0 \frac{VH}{2}$ for clarity's purposes, $|h(a, b)|$ is simply given by

$$|h(a, b)| = \begin{cases} \frac{\|\mathbf{E}_s\|}{\frac{k_0 LH}{R_1 R_2} \sqrt{\frac{P_{TX} G_{TX}(\theta_1) \zeta_0}{32\pi^3}} \|\boldsymbol{\delta}_b\|} & \text{if } \mathbf{s}_r \cdot \mathbf{n} \leq 0 \\ \frac{\|\mathbf{E}_s\|}{\frac{k_0 LH}{R_1 R_2} \sqrt{\frac{P_{TX} G_{TX}(\theta_1) \zeta_0}{32\pi^3}} \|\boldsymbol{\delta}_r\|} & \text{otherwise.} \end{cases} \quad (28)$$

Note that the main limitation of this approach is that $|h|$ can only be simulated on a finite subset of \mathbb{R}^2 . Therefore, for the value of a and b outside of this subset, a constant padding is applied to the $|h|$ function. Denoting $I_a = [a_{min}, a_{max}]$ and $I_b = [b_{min}, b_{max}]$ the intervals on which $|h(a, b)|$ has been determined, $|h|$ is obtained for any point of \mathbb{R}^2 as

$$|h(a, b)| = |h(\psi_a(a), \psi_b(b))| \quad (29)$$

where

$$\begin{aligned} \psi_a(a) &= \begin{cases} \max(a, a_{min}) & \text{if } a < 0 \\ \min(a, a_{max}) & \text{otherwise} \end{cases} \\ \psi_b(b) &= \begin{cases} \max(b, b_{min}) & \text{if } b < 0 \\ \min(b, b_{max}) & \text{otherwise.} \end{cases} \end{aligned} \quad (30)$$

An example of the determination of $|h|$ for the ENAC campus building (see Fig. 4) is provided in the following. The targeted $|h|$ function is denoted as $|h_{ec}|$. To compare the $|h_{ec}|$ function obtained with the smooth and homogeneous case (equation (18)), two properties of $|h_{ec}|$ are investigated:

1. The variable separability of $|h_{ec}|$. A function $|h_{ec}|$ is said to be variable separable if $\forall (\gamma, \beta) \in \mathbb{R}^2$,

$$|h_{ec}(a, b)| = \frac{|h_{ec}(a, \beta)| |h_{ec}(\gamma, b)|}{|h_{ec}(\gamma, \beta)|}. \quad (31)$$

For this study, $\gamma = \beta = 0$ is chosen.

2. The shape of the $|h_{ec}|$ function. In particular, the resemblance between $|h_{ec}|$ and the sinc function is examined.

Variable separability of $|h_{ec}|$: $|h_{ec}|$ is variable separable if and only if $\forall n \in \mathbb{N}^*$ every matrix \mathbf{S} of the form

$$\mathbf{S} = (|h_{ec}(a_p, b_q)|)_{\substack{1 \leq p \leq n \\ 1 \leq q \leq n}} \quad (32)$$

has a rank equal to one, where a_p and b_q are discrete values. For this study, a simulation using (28) was performed to obtain a matrix \mathbf{S} for $n = 8$ ($\mathbf{S} \in \mathcal{M}_8(\mathbb{R})$). It was found that the rank of the obtained matrix was one, with a tolerance threshold on the singular values equal to 10^{-4} . Thus, $|h_{ec}|$ is considered variable separable. This is consistent with the smooth and homogeneous scatterer case (19), where $|h_{ec}(a, b)|$ is simply $|\text{sinc}(a)| |\text{sinc}(b)|$.

Given the variable separability of $|h_{ec}|$, $|h_{ec}(a, b)|$ can be written as

$$|h_{ec}(a, b)| = \frac{|h_{ec}(a, 0)| |h_{ec}(0, b)|}{|h_{ec}(0, 0)|}. \quad (33)$$

This property is also convenient regarded the number of simulations needed since $|h_{ec}|$ can be determined for a full rectangle subset of \mathbb{R}^2 by only performing simulations on two crossing line segments of \mathbb{R} .

Shape of $|h_{ec}|$: Since $|h_{ec}|$ is variable separable, the shape of the four $|h_{ec}(a, 0)|$ and the four $|h_{ec}(0, b)|$ functions (one per material) are investigated separately. In particular, the shape of $|h_{ec}(a, 0)|$ and $|h_{ec}(0, b)|$ are compared to the sinc functions obtained in the smooth and homogeneous case expressed in equation (19). To obtain $|h_{ec}(a, 0)|$ and $|h_{ec}(0, b)|$, the simulations are performed using (28) in the horizontal and in the vertical scene, at the L5 carrier frequency, respectively.

Fig. 6 shows an upper view of the horizontal scene used for the simulations.

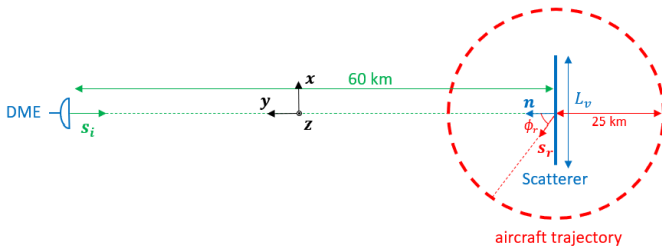
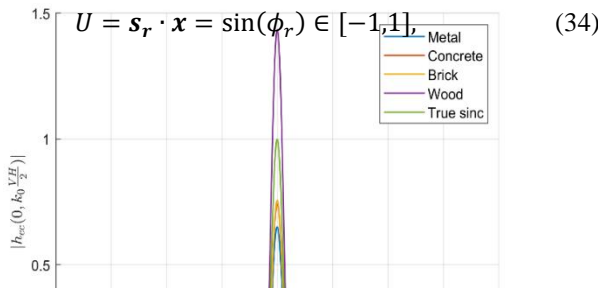


Fig. 6. Upper view of the horizontal scene.

In Fig. 6, the value of b is maintained at 0 by containing the aircraft trajectory in the horizontal plane. The angle ϕ_r represents the angle from the horizontal specular reflection and ranges from $-\pi$ to π along the trajectory. For each position of the aircraft, a value of $|h_{ec}(a, 0)|$ is obtained. Note that since $\mathbf{s}_i \cdot \mathbf{x} = 0$, U is given by



and therefore $I_a = \left[-\frac{k_0^{L5} L_{ec}}{2}, \frac{k_0^{L5} L_{ec}}{2} \right]$ where k_0^{L5} is the wave number for the L5 frequency and $L_{ec} = 69.6$ m is the length of the ENAC campus building facade.

Fig. 7 shows a side view of the vertical scene used for the simulations.

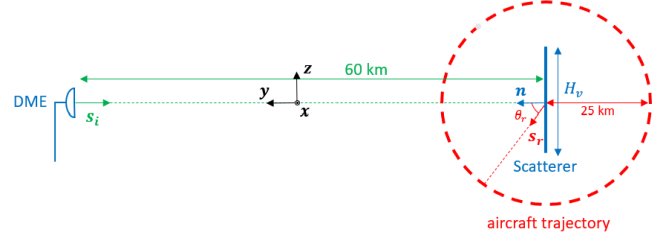


Fig. 7. Side view of the vertical scene.

In Fig. 7, the value of a is maintained at 0 by containing the aircraft trajectory in the vertical plane. The angle θ_r represents the angle from the vertical specular reflection and ranges from $-\pi$ to π along the trajectory. For each position of the aircraft, a value of $|h_{ec}(0, b)|$ is obtained. Note that since $\mathbf{s}_i \cdot \mathbf{z} = 0$, V is given by

$$V = \mathbf{s}_r \cdot \mathbf{z} = \sin(\theta_r) \in [-1, 1], \quad (35)$$

and therefore $I_b = \left[-\frac{k_0^{L5} H_{ec}}{2}, \frac{k_0^{L5} H_{ec}}{2} \right]$ where $H_{ec} = 16.2$ m is the height of the ENAC campus building facade.

The two simulations are performed for the four possible materials (metal, concrete, brick and wood) in presence of glass windows and the simulated $|h_{ec}(a, 0)|$ and $|h_{ec}(0, b)|$ functions using (28) are presented in Fig. 8 and Fig. 9 respectively, where a zoom for $-5^\circ \leq \phi_r \leq 5^\circ$ and $-20^\circ \leq \theta_r \leq 20^\circ$ are performed for visualization purposes.

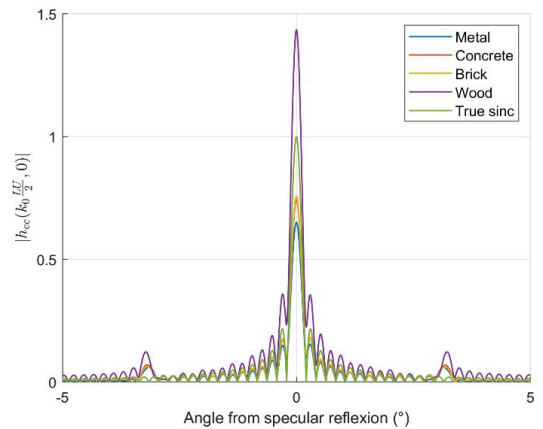


Fig. 8. $|h_{ec}(a, 0)|$ for $-5^\circ \leq \phi_r \leq 5^\circ$ for the four possible dominant materials.

positions, amplitudes and widths of the GL are discussed and the analysis concluded.

Influence of scatterer geometric parameters on the shape of $|h_{ec}|$: The geometric parameters investigated are the scatterer length L and height H , windows length L_w and height H_w , windows vertical and horizontal periodicity L_p and H_p . The initial set of geometric parameters of the ENAC campus building is called the reference set. Table II summarizes the range, the step and the number of values N_{gp} investigated for the geometric parameters. The last column is used to show the reference set of the ENAC campus building.

TABLE II
Range, step, number of values and reference set for the geometric parameters investigated.

Parameter	Start (m)	End (m)	Step (m)	N_{gp}	Ref (m)
L	11.2	69.6	19.5	3	69.6
H	4.8	16.2	2.9	4	16.2
L_w	3.3	7.9	4.6	2	3.3
H_w	1.6	2.8	1.2	2	1.6
L_p	1.3	5.9	4.6	2	1.3
H_p	1.2	2.8	1.6	2	1.2

Three remarks can be made on the $|h_{ec}(a, 0)|$ and $|h_{ec}(0, b)|$ functions:

1. They are similar to the sinc function which is consistent with the smooth and homogeneous case (19).
2. There are Grating Lobes (GL) due to the presence of the periodically distributed windows.
3. The highest peak of $|h_{ec}(a, 0)|$ and $|h_{ec}(0, b)|$ can be smaller or greater than one depending on the material. However, $|h_{ec}(a, 0)|$ and $|h_{ec}(0, b)|$ are later normalized by $|h_{ec}(0, 0)|$ (33) and scaled by \mathbf{R} (20) which both depend on the material. After the normalization and scaling, the maximum and minimum highest peaks are obtained for the metal and the wood, respectively. The values of $|h_{ec}(0, 0)|$ for the 5 different materials is provided in the last column of Table I.

To summarize, both the $|h_{ec}(a, 0)|$ and $|h_{ec}(0, b)|$ functions obtained in the case of the ENAC campus building can be seen as the sum of a background sinc function with a function g generating the GL.

B. Addressing Limitation 1

Limitation 1 concerns the precise knowledge of the composition of the facades. Considering the very high number of scatterers that have to be considered for the proposed AG propagation channel model, it is extremely challenging to obtain such information.

In this section, Limitation 1 is addressed by showing that for all the scatterers in the scenario, equation (27) can be used with the $|h|$ function of a single reference scatterer but customized for the scatterer dimensions, dominant material and a and b values from a statistical point of view. First, it is shown that not only the $|h_{ec}|$ function from the ENAC campus building but any function $|h|$ from any rectangular scatterer is a sum of background sinc function with a function g generating the GL, where the positions, amplitudes and widths of the GL depend on the scatterer geometric parameters, by investigating the shape of $|h_{ec}|$ when the geometric parameters of the ENAC campus building are modified. Second, the importance of the

The geometric parameters are investigated individually. Two simulations are performed each time a geometric parameter is modified from the initial set of parameters of the ENAC campus building and the impact on the $|h_{ec}|$ shape is investigated. The two scenes considered for the two simulations are the vertical and horizontal scenes presented in Fig. 6 and Fig. 7. For illustration purposes, Fig. 10 presents the $|h_{ec}(0, b)|$ normalized function for metal with (a) $H = 10.4$ m and (b) $H_p = 2.8$ m in comparison with the $|h_{ec}(0, b)|$ function of the ENAC campus building with its reference set of parameter and the perfect sinc function of a smooth and homogeneous scatterer with the dimension of the ENAC campus building. Other simulations results are not shown in this paper for the sake of conciseness.

The simulation results show that the modification of the geometric parameters of the scatterers impacts the position, width and amplitude of the grating but that both $|h_{ec}(a, 0)|$ and $|h_{ec}(0, b)|$ functions can still be seen as the sum of a background sinc function with a function g generating the GL.

Therefore, it is assumed that not only the ENAC campus building but for any other rectangular facade with different set of geometric parameters, the functions $|h(a, 0)|$ and $|h(0, b)|$ of this scatterer can be considered as a sum of a sinc function (which mainly depends on the scatterer height and length) with another function representing the GL.

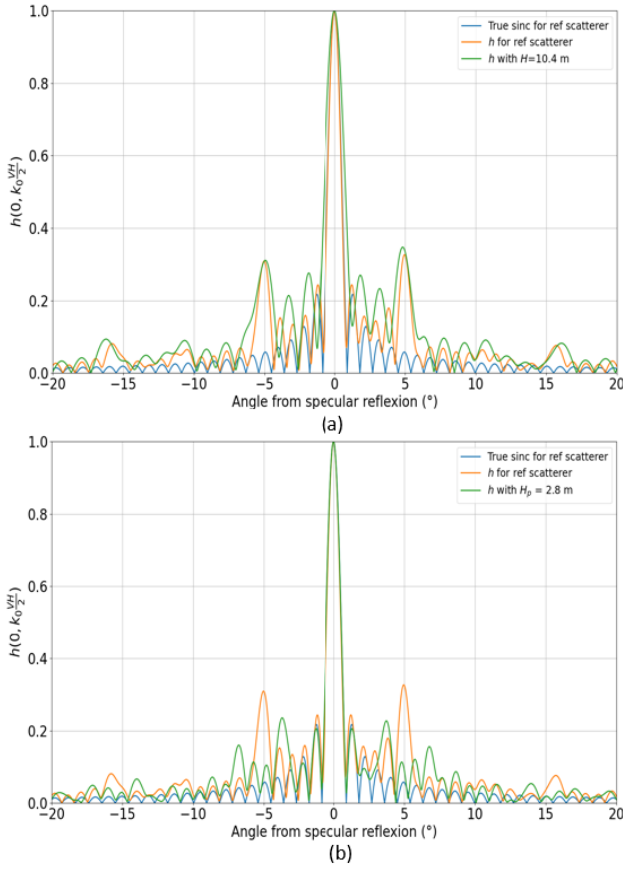


Fig. 10. $|h_{ec}(0, b)|$ normalized function for metal with (a) $H = 10.4$ m and (b) $H_p = 2.8$ m (in blue) in comparison with the $|h_{ec}(0, b)|$ function of the ENAC campus building (in orange) and a perfect sinc (in green).

Discussion: GL have three characteristics: position, width and amplitude. These parameters depends on the scatterer windows' height, length and horizontal and vertical periodicity [30] and therefore on the scatterer specific geometric parameters. However, considering the very high number of scatterers present in the scenario, all these scatterers can be represented by the $|h_{ec}|$ ENAC campus building campus from a statistical point of view, for 3 reasons:

1. With such a high number of scatterers, the horizontal orientation of the scatterers can be assumed to be uniform on $[0, 2\pi[$ and thus the positions of the GL in any $|h(a, 0)|$ do not matter: the probability to fall into a GL is independent from the positions of the GL.
2. The vertical orientation of the scatterers can not be assumed to be uniform on $[0, 2\pi[$ given the configuration. However, the vertical orientation is assumed to be contained in $[0, 10^\circ]$. In this interval, a GL is present in the $|h_{ec}(0, b)|$ function (see Fig. 9) which represent a worst-case scenario since no GL could be present at all for the $|h|$ function of other scatterers.
3. The width and amplitude of the GL depend on the windows dimension and periodicity. Since the ENAC campus building windows are assumed to be representative of a typical building, the width and

amplitude of the GL of ENAC campus building $|h_{ec}(a, 0)|$ and $|h_{ec}(0, b)|$ functions are assumed to be representative of an average case.

Therefore, it is concluded that the ENAC campus building $|h_{ec}(a, 0)|$ and $|h_{ec}(0, b)|$ functions can be used for any scatterer considered in the scenario from a statistical point of view. Combining this approach with the simplified scattered field $\widetilde{\mathbf{E}}_s$, the knowledge of the facades is no longer needed and thus both Limitation 1 and 2 are addressed.

C. Scattered Power P and Necessary Inputs For The Propagation Channel Model

Combining the tackling of Limitation 1 and 2 and using equation (22), the scattered power P is updated into

$$P = \begin{cases} \widetilde{P}^0 \|\delta_b\|^2 & \text{if } \mathbf{s}_r \cdot \mathbf{n} \leq 0 \\ \widetilde{P}^0 \|\delta_r\|^2 & \text{otherwise,} \end{cases} \quad (36)$$

with

$$\begin{aligned} \widetilde{P}^0 &= \frac{L_H P_{TX} G_{TX}(\theta_1) G_{RX}(\theta_2)}{\lambda^2 R_2^2} (LH)^2 \cdot \\ &\frac{\left| h_{ec}\left(\phi_a\left(k_0 \frac{UL}{2}\right), 0\right) \right|^2 \left| h_{ec}\left(0, \phi_b\left(k_0 \frac{VH}{2}\right)\right) \right|^2}{|h_{ec}(0, 0)|^2}. \end{aligned} \quad (37)$$

To summarize, after applying the SSPO approach, only four scatterers' inputs are necessary to determine the additional delay τ and the scattered power P necessary to completely determine the proposed propagation channel from a RFI impact analysis point of view::

1. The position of the center of the scatterers, that is needed to derive R_1, R_2 and many other parameters,
2. The dimensions L and H of the scatterers, that are directly used in (37),
3. The orientation of the obstacles, which is used in δ_b and δ_r (20),
4. The material composition of the scatterer, which is needed for the derivation of \mathbf{R} and the choice of $|h_{ec}|$.

V. METHODOLOGY FOR THE C/N_0 DEGRADATION CONSIDERING MP

In this section, the global methodology to derive the C/N_0 degradation in presence of MP for any aircraft position is presented. The methodology consists of 4 steps.

Step 1 - Determination of the Visible Beacons and Their RLOS: the visible DME/TACAN beacons are determined in the RLOS of the aircraft. The aircraft or the DME/TACAN beacon RLOS is derived from (2).

Step 2 - Determination of the Visible Scatterers Within the RLOS and Their Four Necessary Inputs: the N scatterers and their four necessary inputs (position, dimension, orientation and composition) within the RLOSs are determined from

external sources such as large data bases. Note that some of the scatterers inputs might have to be stochastically generated, depending on the information available for the scatterers at the DME/TACAN beacons location.

Step 3 – Determination of the Okumura-Hata Environment: From the position, length and orientation of the scatterers, the obstructed scatterers are identified. The non-obstructed scatterer are assumed to follow the Okumura-Hata open path loss as described in Section III.B. For the obstructed scatterers, the Okumura-Hata environment is either urban or suburban and is arbitrary chosen after looking at the scatterer environment in external sources.

Step 4 - Application of the Proposed AG Channel Model: the proposed wideband AG channel model is applied to the scatterers within the RLOS of the visible DME/TCAN beacons. From the propagation channel, the additional delay with respect to the LOS of the MP τ (7) and the MP scattered power P (37) are retrieved for each of the scatterers.

Step 5 - Application of the C/N_0 Degradation Model Considering Multipath: the C/N_0 degradation model due to DME/TACAN considering MP developed in [5] is applied. The C/N_0 degradation is given by

$$\left(\frac{C}{N_0}\right)_{deg} = 10 \log_{10} \left(\frac{1 - bdc}{1 + R_I} \right), \quad (38)$$

where bdc is the blanking duty cycle,

$$bdc = 1 - e^{-2 \sum_{m=1}^M length(U_{s=1}^{S_m} B_m^S) \cdot PRF_m}, \quad (39)$$

with M the number of DME/TACAN beacons, S_m the number of disjoint blanked intervals generated by the beacon m , $B_m^S = [B_m^{S,l}, B_m^{S,r}]$ the m^{th} disjoint blanked interval and PRF_i the pulse repetition frequency for beacon i . The below-blanker interfering signal-to-noise-ratio R_I is given by

$$R_I = \sum_{m=1}^M \frac{SSC(\Delta f_m) PRF_m \sqrt{\pi/\alpha}}{N_0 \beta_0} \sum_{n=1}^{N_m} P_m^n \left\{ 2 \left(1 - \mathbf{1}_{I_m^{bdc}}(\tau_m^n) \right) + \sum_{s=1}^{S_m} \left[\frac{\text{sign}(\tau_m^n - B_m^{S,l})^{1 - \mathbf{1}_{B_m^S}(\tau_m^n)} \text{erfc}(\sqrt{\alpha} |B_m^{S,l} - \tau_m^n|) + \text{sign}(B_m^{S,r} - \tau_m^n)^{1 - \mathbf{1}_{B_m^S}(\tau_m^n)} \text{erfc}(\sqrt{\alpha} |B_m^{S,r} - \tau_m^n|) \right] \right\}, \quad (40)$$

where SSC is the Spectral Separation Coefficient of beacon m , N_0 is the thermal noise power spectrum density level generated by the Radio-Frequency Front End (RFFE) block, β_0 is the thermal noise power degradation due to RFFE filter and correlator, N_m is the number of scatterers in the RLOS of beacon m , P_m^n and τ_m^n are the scattered power and the additional delay generated by scatterer n of beacon m respectively, $\mathbf{1}$ is the indicator function and I_m^{bdc} is the total blanked interval generated by beacon m . The reader is referred to [5] for a more thorough explanation.

VI. APPLICATION TO JALTO AND TIXAK

In this section, the C/N_0 degradation due to DME/TACAN considering MP is derived by applying the methodology presented in section V at the two low altitude operational hot-spots defined during the RTCA Working Group 6 (WG6) activities [32]. The section is organized as follows. Section IV.A briefly introduces the criterion applied by the RTCA WG6 to identify the two altitude operational hot-spots. Section IV.B presents the visible beacons and their RLOS. In Section IV.C the choices of definition of the four necessary inputs of the scatterers within the RLOSs are introduced. Section IV.D is dedicated to the presentation and analysis of the results obtained applying the proposed AG channel and C/N_0 degradation models.

A. Identification of The Operational Low Altitude Hot-Spots

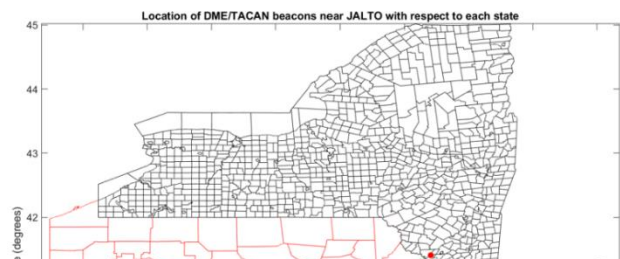
In the course of the RTCA WG6 activities, the operational low altitude hot spots for US and Europe have been determined finding the closest operational waypoint to the worst C/N_0 degradation due to DME/TACAN without considering MP at low altitude. Using this criterion, the following hot-spots were identified:

1. The US operational low altitude hot-spot: JALTO, flight altitude 2100ft AGL (altitude 640m), situated in Pennsylvania, near Philadelphia.
2. The European operation low altitude hot-spot: TIXAK, flight altitude 2000ft AGL (altitude 609m), situated in Germany, near Frankfurt.

B. Determination of The Visible DME/TACAN Beacons And Their RLOSs

At JALTO, 19 DME/TACAN beacons are identified inside the aircraft RLOS. The DME/TACAN beacons are dispatched in 5 different states: 6 in Pennsylvania, 10 in New Jersey, 1 in New York, 1 in Delaware and 1 in Maryland. The height of the DME/TACAN beacons' antenna is retrieved from a 2022 Federal Aviation Administration (FAA) database. The mean of the RLOS obtained for the 19 DME/TACANs beacons is 24.73 km, with a very low standard deviation. Fig. 11 shows a map of JALTO and the visible DME/TACAN beacons in the 6 different states, where the aircraft is situated at the blue dot.

At TIXAK 13 DME/TACAN beacons are identified inside the aircraft RLOS. The DME/TACAN beacons are dispatched in 2 countries: 12 in Germany and 1 in Luxembourg. The height of the DME/TACAN beacons' antenna is retrieved from a 2022 EUROCONTROL database. The mean of the RLOS obtained for the 13 DME/TACANs beacons is 23.14 km, with a very low standard deviation. Fig. 12 shows a map of TIXAK and the visible DME/TACAN beacons, where the aircraft is situated at the blue dot.



consecutive corners of a 2D-building facade, the position \mathbf{M} of the center of a scatterer is given by

$$\mathbf{M} = (\mathbf{F} - \mathbf{E})/2, \quad (41)$$

the length L of the scatterer is

$$L = \|\mathbf{F} - \mathbf{E}\|^2 \quad (42)$$

and the horizontal orientation ϕ_p , the angle between \mathbf{n} and \mathbf{x} is

$$\phi_p = \begin{cases} \text{acos}(\mathbf{x} \cdot \mathbf{n}) & \text{if } \mathbf{n} \cdot \mathbf{y} \geq 0 \\ 2\pi - \text{acos}(\mathbf{x} \cdot \mathbf{n}) & \text{otherwise.} \end{cases} \quad (43)$$

Determination of scatterers height: For JALTO, no database was found for the height of the scatterers. Therefore, an arbitrary value $H = 8$ m was chosen, which represents a tradeoff between the numerous country-side two-story building ($H \approx 5$ m) and the small amount of large ten-story buildings ($H \approx 30$ m) from the city centers.

For TIXAK, an European publicly available database provided by Copernicus [35] was used to retrieve the height H of the scatterers. Since the database only provides the height of the scatterers within the major European cities, for the other scatterers the height was arbitrarily chosen to 5 m (two-story building).

Determination of the scatterers composition: The proposed AG channel model is intended to work with a database of the scatterers material composition. However, at the epoch of the article's writing, no accurate database was found for the scatterers composition for JALTO and TIXAK. Therefore, for both hot spots, the composition of the scatterers are arbitrarily chosen through 5 different composition scenarios (CS) defined from the close observation of the DME/TACAN beacons surroundings in Google Maps. Indeed, 5 different scenarios are analyzed to assess the impact of the materials on the C/N_0 degradation as well as to show a potential worst case scenario (when the highest number of buildings made of metal is assumed) and a more realistic scenario (scenario 5).

A CS is defined as a distribution of the scatterers material. The distribution of the materials is used to randomly assign a material to each identified scatterer. Table III and Table IV provide the proposed distribution for the first four scenarios for JALTO and TIXAK respectively, where "Wd" stands for wood, "Crt" for concrete, "Mtl" for metal and "Brk" for brick. The main difference between JALTO and TIXAK CSs is that the wood is transformed into brick for TIXAK, since wood houses present in the US are not found in Europe where the brick is more often employed.

TABLE III

Material distribution for the first four scenarios, JALTO

	Length ≤ 50 m	Length > 50 m	O-H
--	--------------------	-----------------	-----

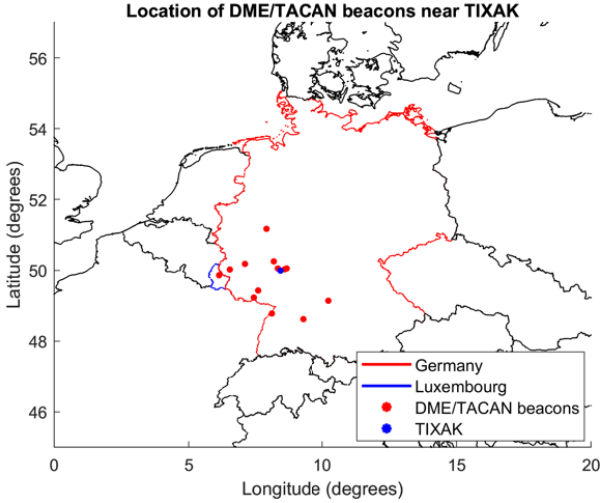


Fig. 12. TIXAK, the low altitude EU operational hot-spot and the visible DME/TACAN beacons.

C. Determination of The Four Scatterers Inputs and Okumura-Hata environments

In this section, the determination of the N_m scatterers for each of the visible DME/TACAN beacons and their four necessary inputs for the application of the proposed AG channel model for both JALTO and TIXAK is presented. Note that the dimension parameter is divided into two parameters, length and height, for this section.

Determination of the scatterers position, orientation and length: For JALTO and TIXAK, the positions, orientations and lengths of the scatterers are retrieved from a worldwide computer-generated and publicly available database of the building footprints (horizontal plane projection only) released by Microsoft [34]. In total, more than 23 million and 15 millions of building facades are found for JALTO and TIXAK, respectively. Denoting \mathbf{E} and \mathbf{F} the coordinates of two

	Wd (%)	Crt (%)	Mtl (%)	Wd (%)	Crt (%)	Mtl (%)	
CS 1	40	40	20	40	40	20	S
CS 2	45	45	10	45	45	10	S
CS 3	50	50	0	0	50	50	S
CS 4	50	50	0	0	70	30	S

TABLE IV

Material distribution for the first four scenarios, TIXAK

	Length $\leq 50 m$			Length $> 50 m$			O-H
	Brk (%)	Crt (%)	Mtl (%)	Brk (%)	Crt (%)	Mtl (%)	
CS 1	40	40	S	40	40	20	S
CS 2	45	45	S	45	45	10	S
CS 3	50	50	S	0	50	50	S
CS 4	50	50	S	0	70	30	S

In CS 1 and 2, there is no difference between the distribution for small ($L \leq 50m$) and large ($L > 50m$) obstacles for both JALTO and TIXAK. They are the simplest scenarios and the ones where the most metal is assumed to be present. Only a small change on the metal composition differentiates the two scenarios.

In CS 3 and 4, a difference is made between small and large obstacles for the compositions of the materials for both JALTO and TIXAK. This was deemed necessary since the largest scatterers are mostly made of concrete and metals (warehouses, commercial centers, hospitals, penitential centers, etc.) whereas smaller obstacles are mostly made of concrete, brick and wood (residential houses, small farms, etc.). Only a small change on the metal composition differentiates the two scenarios.

CS 5 is the most evolved scenario. It relies on the definition of four different zones for JALTO, and three zones for TIXAK. Each DME/TACAN beacon is assigned to a zone before running the simulations.

Zone 1 represents the urban environment. It is associated with large cities such as Philadelphia and Frankfurt for JALTO and TIXAK, respectively. The composition is mostly made of concrete and brick given the presence of large buildings.

Zone 2 represents the suburban environment. The composition is mostly made of wood for JALTO and brick for TIXAK given the presence of numerous houses in large residential areas.

Zone 3 represents the rural environment. The composition is mostly made of wood for JALTO and brick for TIXAK given the dominance of allotments.

Zone 4 is only available for JALTO and represents the coastal environment. The scatterers are mostly made of wood.

Table IV and Table V provides the proposed distributions for the scenario 5 for JALTO and TIXAK, respectively.

TABLE V

Material distribution for scenario 5, JALTO

	Length $\leq 50 m$	Length $> 50 m$	O-
--	--------------------	-----------------	----

	Wd (%)	Crt (%)	Brk (%)	Mtl (%)	Wd (%)	Crt (%)	Brk (%)	Mtl (%)	H
Z1	45	5	45	5	2	35	55	8	U
Z2	55	5	35	5	5	45	45	5	S
Z3	65	5	25	5	8	55	35	2	O
Z4	80	5	10	5	20	50	15	15	S

TABLE VI

Material distribution for scenario 5, TIXAK

	Length $\leq 50 m$				Length $> 50 m$				O-H
	Wd (%)	Crt (%)	Brk (%)	Mtl (%)	Wd (%)	Crt (%)	Brk (%)	Mtl (%)	
Z1	5	65	25	5	2	65	25	8	U
Z2	5	55	35	5	5	55	35	5	S
Z3	5	45	45	5	8	45	45	2	O

Determination of the Okumura-Hata Environments: From the position, length and orientation of the scatterers, the obstructed and non-obstructed scatterers are identified. The Okumura-Hata environment of obstructed scatterers is defined for the 5 scenarios after the close observation of the beacon surrounding in Google Maps for both JALTO and TIXAK in the last column of Table III, Table IV, Table V and Table VI where “O-H” stands for Okumura-Hata, “O” for open, “S” for suburban and “U” for urban.

D. Application of the Proposed AG Channel Model

Knowing the four necessary inputs of each scatterer, the proposed AG channel model is applied to obtain the scattered power P (36) and the additional delay τ (7) generated by each scatterer associated to each individual DME/TACAN beacon. Fig. 13 provides the scattered power occurrence as a function of the additional delay with respect to the LOS signal Δ_τ obtained for (a) the beacon 5 and (b) the beacon 14 of JALTO, respectively. The blanking threshold (when visible) is represented by a red line. The number of scatterers N_m ($m = 5$ or $m = 14$) and LOS power are provided in the title.

Three remarks can be made regarding Fig. 13:

1. The power scattered by the obstacle is at least 20 dB and majority around 100 dB below the LOS power. This is due to the Okumura-Hata path loss, the scattering and the $|h_{ec}|$ function as defined in Section IV.A.
2. Even if the scattered power generated by the individual scatterer is usually very low, the number of scatterers is very high and an impact is expected on R_f .
3. When the LOS power is high, a very few number of scattered powers can be above the blanking threshold (see beacon 5 for example).

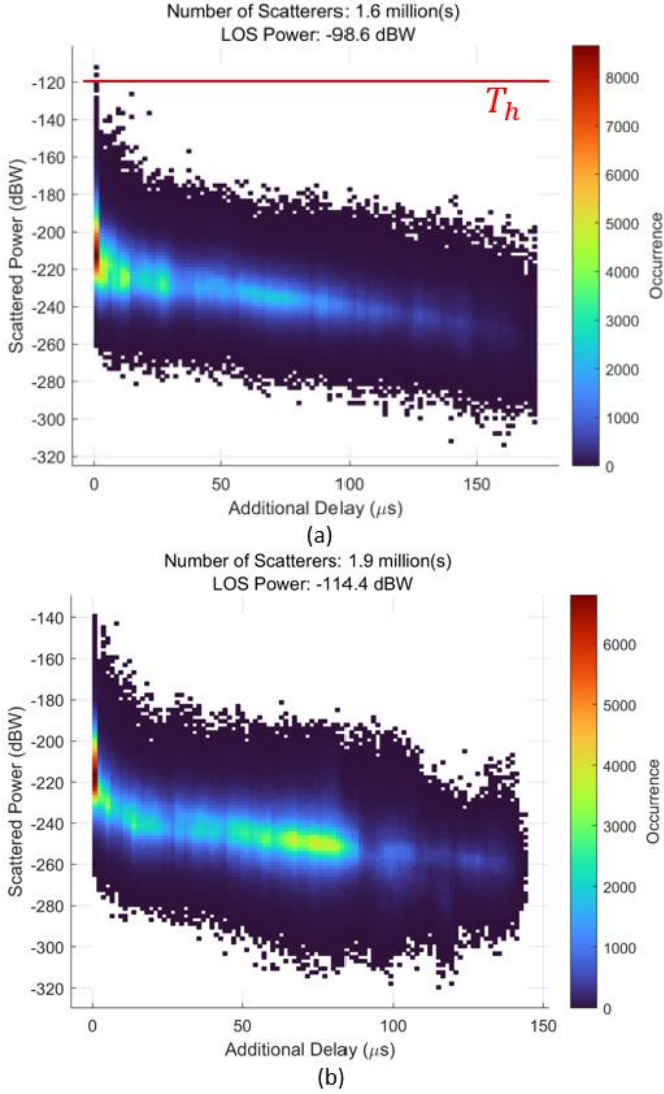


Fig. 13. scattered power occurrence over the additional delay obtained for (a) the beacon 5 and (b) the beacon 14
E. Application of the C/N_0 degradation Model

With P and τ for every visible scatterers, R_I (40) and bdc (39) are determined and the C/N_0 (38) degradation due to DME/TACAN considering MP is obtained. Since the facades compositions are chosen randomly, the process is repeated 20 times and the mean and standard deviation (std) of R_I , bdc and C/N_0 are provided. The results of the simulation are presented for JALTO in Table VII and Table VIII and for TIXAK in Table IX and Table X for $BW = 16$ MHz and $BW = 20$ MHz, respectively. The C/N_0 degradation in multipath-free conditions is presented in the last lines of Table VII and Table VIII for JALTO and Table IX and Table X for TIXAK for comparison purposes.

TABLE VII

C/N_0 degradation at JALTO considering MP, $BW = 16$ MHz

JALTO	R_I (-)		bdc (-)		$\left(\frac{c}{N_0}\right)_{deg}$ (dB)	
	Mean	std	Mean	std	Mean	std
Scenario 1	0.22	0.01	0.27	0.00	2.3	0.04
Scenario 2	0.23	0.02	0.27	0.00	2.32	0.05
Scenario 3	0.23	0.01	0.28	0.00	2.29	0.04
Scenario 4	0.22	0.01	0.28	0.00	2.27	0.03
Scenario 5	0.24	0.01	0.27	0.00	2.31	0.03
Without MP	0.16		0.27		2.00	

TABLE VIII

C/N_0 degradation at JALTO considering MP, $BW = 20$ MHz

JALTO	R_I (-)		bdc (-)		$\left(\frac{c}{N_0}\right)_{deg}$ (dB)	
	Mean	std	Mean	std	Mean	std
Scenario 1	0.23	0.0132	0.32	0.00	2.59	0.03
Scenario 2	0.22	0.01	0.32	0.00	2.56	0.03
Scenario 3	0.23	0.01	0.32	0.00	2.59	0.02
Scenario 4	0.23	0.01	0.32	0.00	2.57	0.02
Scenario 5	0.24	0.01	0.32	0.00	2.62	0.03
Without MP	0.17		0.31		2.30	

TABLE IX

C/N_0 degradation at TIXAK considering MP, $BW = 16$ MHz

TIXAK	R_I (-)		bdc (-)		$\left(\frac{c}{N_0}\right)_{deg}$ (dB)	
	Mean	std	Mean	std	Mean	std
Scenario 1	0.17	0.03	0.19	0.00	1.59	0.05
Scenario 2	0.16	0.02	0.19	0.00	1.56	0.04
Scenario 3	0.15	0.00	0.19	0.00	1.53	0.01
Scenario 4	0.15	0.00	0.19	0.00	1.53	0.01
Scenario 5	0.15	0.00	0.19	0.00	1.53	0.01
Without MP	0.13		0.19		1.45	

TABLE X

C/N_0 degradation at TIXAK considering M, $BW = 20$ MHz

TIXAK	R_I (-)		bdc (-)		$\left(\frac{c}{N_0}\right)_{deg}$ (dB)	
	Mean	std	Mean	std	Mean	std
Scenario 1	0.18	0.04	0.23	0.00	1.84	0.05
Scenario 2	0.17	0.03	0.23	0.00	1.80	0.04
Scenario 3	0.16	0.00	0.23	0.00	1.75	0.01
Scenario 4	0.15	0.00	0.23	0.00	1.73	0.01
Scenario 5	0.15	0.00	0.23	0.00	1.74	0.01
Without MP	0.13		0.23		1.65	

Three conclusions are extracted from the results:

1. The range of the additional C/N_0 degradation generated by the DME/TACAN MP ranges from 0.26 to 0.32 dB at JALTO and from 0.08 to 0.19 dB at TIXAK, where less scatterers are visible.

2. The impact of the MP on bdc is almost always null, except for JALTO where it reaches at most 0.01. This means that very few building facades are generating a scattered power above the blanking threshold. Note that other scatterer type that could have triggered the blanker, such as radios antennas or electric pylons, have not been considered in this analysis.
3. R_f is the parameter most impacted by the consideration of MP due to the very high number of scatterers generating a scattered power below the blanking threshold in the DME/TACAN beacon RLOS.

VII. CONCLUSION

In this article, a new hybrid determinist-stochastic geometrically based wideband AG propagation channel model have been proposed. The proposed AG model includes an analytical formula for the additional delay, an Okumura-Hata path loss for the scatterer illumination and the mathematical expression of the scattered power generated by the scatterers using a statistical simplification of the classic PO approach to allow the model to cope with very large numbers of scatterers present in the scenarios. After the application of the SSPO approach, only four inputs are needed from the scatterers to apply the proposed AG model: the position, dimension, orientation and composition. It must be highlighted that the proposed AG channel is neither restricted to the RFI analysis, since the CIR time series can almost be generated (accounting for a phase mathematical model) nor to the DME/TACAN system; the proposed AG channel model could be applied to any other system composed of a ground emitter and a sky receiver operating in the L-band.

Combining the proposed channel model with the C/N_0 degradation model presented in Part I, the general methodology to determine the C/N_0 due to DME/TACAN considering MP have been determined. To illustrate the application of these models, the analysis of two cases of study, JALTO, in the US, and TIXAK, in Europe, have been conducted. In this article, the heights of the scatterers have been arbitrarily chosen and, although the channel model is intended to work with a deterministic environment, the compositions of the scatterers have been stochastically determined due to the lack of information about scatterers materials composition. Note that this stochastic element is to be removed as soon as precise databases concerning the scatterers material composition are available. Results have shown that the consideration of MP adds to the C/N_0 degradation due to DME/TACAN from 0.26 to 0.32 dB and from 0.08 to 0.19 dB at JALTO and TIXAK (where less scatterers are visible), respectively.

REFERENCES

- [1] RTCA, "DO 292 - Assessment of Radio Frequency Interference Relevant to the GNSS L5/E5A Frequency Band," Jul. 2004. [Online].
- [2] F. Bastide, "Analysis of the Feasibility and Interests of Galileo E5a/E5b and GPS L5 for Use with Civil Aviation," Institut National Polytechnique de Toulouse, France, 2004.
- [3] C. Hegarty, T. Kim, S. Ericson, P. Reddan, T. Morrissey, and A. J. Van Dierendonck, "Methodology for Determining Compatibility of GPS L5 with Existing Systems and Preliminary Results," presented at the Proceedings of The Institute of Navigation Annual Meeting, Cambridge, MA, Jun. 1999.
- [4] C. Hegarty, A. J. Van Dierendonck, D. Bobyn, M. Tran, T. Kim, and J. Grabowski, "Suppression of Pulsed Interference through Blanking," presented at the Proceedings of the Institute of Navigation Annual Meeting, Fairfax, VA, Jun. 2000.
- [5] N. Gault, A. Garcia-Pena, A. Chabory, and C. Macabiau, "DME/TACAN Multipath Impact on GNSS L5/E5a Airborne Receivers Part I: C/N_0 Degradation Model," *IEEE Trans. Aerosp. Electron. Syst.*, submitted.
- [6] D. W. Matolak and R. Sun, "Unmanned aircraft systems: Air-ground channel characterization for future applications," *IEEE Trans. Veh. Technol.*, vol. 10, pp. 79–85, 2015.
- [7] A. Altaf Khuwaja, Y. Chen, N. Zhao, M.-S. Alouini, and P. Dobbins, "A Survey of Channel Modeling for UAV Communications," *IEEE Communications Surveys & Tutorials*, Vol. 20, No. 4, Fourth Quarter 2018.
- [8] J. Khawara, I. Guvenc, D. W. Matolak, U.-C. Fiebig, and N. Scheckenburger, "A survey of air-to-ground propagation channel modeling for unmanned aerial vehicles," *IEEE Commun. Surveys Tuts.*, vol. 21, no. 3, pp. 2361–2391, 3rd Quart 2019.
- [9] C. Yan, J. Zhang, and J. Wang, "A Comprehensive Survey on UAV Communication Channel Modeling," *IEEE Access*, vol. 7, pp. 107769–107792, 2019.
- [10] D. W. Matolak and R. Sun, "Air-ground channel characterization for unmanned aircraft systems—Part I: Methods, measurements, and models for over-water settings," *IEEE Trans. Veh. Technol.*, vol. 66, no. 1, pp. 26–44, Jan. 2017.
- [11] D. W. Matolak and R. Sun, "Air-ground channel characterization for unmanned aircraft systems—Part II: Hilly and mountainous settings," *IEEE Trans. Veh. Technol.*, vol. 66, no. 3, pp. 1913–1925, Mar. 2017.
- [12] D. W. Matolak and R. Sun, "Air-ground channel characterization for unmanned aircraft systems—Part III: The suburban and near-urban environments," *IEEE Trans. Veh. Technol.*, vol. 66, no. 8, pp. 6607–6618, Aug. 2017.
- [13] N. Scheckenburger *et al.*, "Measurement of the L-band air-to-ground channel for positioning applications," *IEEE Trans. Aerosp. Electron. Syst.*, vol. 52, no. 5, pp. 2281–2297, Oct. 2016.

- [14] N. Scheckenburger, T. Jost, M. Walter, G. Del Galdo, D. W. Matolak, and U.-C. Fiebig, "Wideband Air-Ground Channel Model for a Regional Airport Environment," *IEEE Trans. Veh. Technol.*, vol. 68, no. 7, pp. 6243–6256, Jul. 2019.
- [15] E. Haas, "Aeronautical channel modeling," *IEEE Trans. Veh. Technol.*, vol. 51, no. 2, pp. 254–264, Mar. 2002.
- [16] A. Al-Hounani, S. Kandeepan, and A. Jamalipour, "Modeling Air-to-Ground Path Loss for Low Altitude Platforms in Urban Environments," presented at the Proc. IEEE Global Commun. Conf. (GLOBECOM), Austin, TX, USA, 2014, pp. 2898–2904.
- [17] W.-G. Newhall and J. H. Reed, "A geometric air-to-ground radio channel model," presented at the Proc. IEEE Military Commun. Conf. (MILCOM), Anaheim, CA, USA, Oct. 2002, pp. 632–636.
- [18] M. Ibrahim and H. Arslan, "Air-ground Doppler-delay spread spectrum for dense scattering environments," presented at the Proc. IEEE Military Commun. Conf. (MILCOM), Tempa, FL, USA, Oct. 2015, pp. 1661–1666.
- [19] N. Scheckenburger, T. Jost, D. Shutin, M. Walter, G. Del Galdo, and U.-C. Fiebig, "Reflector localization for geometrical modeling the air-ground channel," *IEEE Trans. Veh. Technol.*, vol. 67, no. 9, pp. 7994–8008, Sep. 2018.
- [20] N. Scheckenburger, "Wideband Air-Ground Channel Model for a Regional Airport Environment," Ph.D dissertation, Fakultät für Elektrotechnik und Informationstechnik, Illmenau, Germany, 2017.
- [21] A. Chen, "Development of a Hybrid Deterministic-Statistical GPS Multipath Simulator for Airport Navigation," PhD Thesis, Institut National Polytechnique de Toulouse, 2011.
- [22] M. Ait Ighil, "Enhanced physical-statistical simulator of the land mobile satellite channel for multipath modelling applied to satellite navigation systems," Institut Supérieur de l'Aéronautique et de l'Espace (ISAE), Toulouse, France, 2013.
- [23] M. Ait-Ighil *et al.*, "Simplifying the propagation environment representation for LMS channel modelling," *EURASIP J. Wireless Commun. Netw.*, vol. 1, pp. 1–20, Mar. 2012.
- [24] N. Gault, A. Garcia-Pena, A. Chabory, and C. Macabiau, "Impact of DME/TACAN on GNSS L5/E5a Receiver at Low Altitude Considering Multipath," presented at the Proceedings of the 35th International Technical Meeting of the Satellite Division of the Institute of Navigation (ION GNSS+ 2022), Denver, Sep. 2022.
- [25] M. Hata, "Empirical Formula for Propagation Loss in Land Mobile Radio Services," *IEEE Trans. Veh. Technol.*, vol. 29, no. 3, pp. 317–325, Aug. 1980.
- [26] F. Perez-Fontan and P. M. Espiñeira, *Modelling the Wireless Propagation Channel: A simulation approach with MATLAB*. Wiley, 2008.
- [27] ITU-R P834-9, *Effects of tropospheric refraction on radiowave propagation*. 2017.
- [28] L. Diaz and T. Miligan, *Engineering Using Physical Optics. Practical CAD Techniques and Software*. in Artech House. 1996.
- [29] A. Steingass, A. Lehner, F. Perez-Fontan, E. Kubista, and B. Arbesser-Rastburg, "Characterization of the aeronautical satellite navigation channel through high-resolution measurement and physical optics simulation," *Int. J. Satell. Commun. Netw.*, vol. 26, pp. 1–30, 2008.
- [30] H. Visser, *Antenna Theory and Applications*. Wiley, 2012.
- [31] A. Chabory, "Modélisation Electromagnétique des radômes par des techniques basées sur les faisceaux gaussiens," Paul Sabatier University, Toulouse, France, 2004.
- [32] R. F. Harrington, *Time-Harmonic Electromagnetic Field*. in Wiley. 1961.
- [33] "RTCA Special Committees 159." [Online]. Available: <https://www.rtca.org/sc-159/>
- [34] Microsoft Maps, "Worldwide building footprints." [Online]. Available: <https://github.com/microsoft/GlobalMLBuildingFootprints>
- [35] Copernicus, "Building Height." [Online]. Available: <https://land.copernicus.eu/local/urban-atlas/building-height-2012?tab=mapview>

Nicolas Gault graduated as an electronic engineer from ENAC (École Nationale de l'Aviation Civile) Toulouse, France, in 2020. He is now a Ph.D student at the TELECOM lab of ENAC. His Ph.D topic deals with the model of impact of interferences on the GNSS L5/E5a band. He recently spent 6 months at the RF & SatNav laboratory of the University of Colorado, Boulder, for collaborative research.

Alexandre Chabory received the M.Sc. degree in electrical engineering from ENAC, the French Civil Aviation University, Toulouse, in 2001, and the Ph.D. degree from Paul Sabatier University, Toulouse, in 2004. From 2004 to 2007, he was a Post-Doctoral Scientist with the Eindhoven University of Technology, the Netherlands. Since 2007, he has been with ENAC where he is now full-professor and heading the electromagnetics and antennas research group. His research interests include electromagnetic theory and modeling, mainly for aeronautical applications.

Axel Garcia-Pena is a researcher/lecturer with the SIGNAL processing and NAVigation (SIGNAV) research axis of the TELECOM lab of ENAC (French Civil Aviation University), Toulouse, France. His research interests are GNSS navigation message demodulation, optimization and design, GNSS receiver design and GNSS satellite payload. He received his double engineer degree in 2006 in digital communications from SUPAERO and UPC, and his PhD in 2010 from the Department of Mathematics, Computer Science and Telecommunications of the INPT (Polytechnic National Institute of Toulouse), France.

Christophe Macabiau graduated as an electronics engineer in 1992 from the ENAC (Ecole Nationale de l'Aviation Civile) in Toulouse, France. Since 1994, he has been working on the application of satellite navigation techniques to civil aviation. He received his Ph.D in 1997 and has been in charge of the signal processing lab of ENAC since 2000, where he also started dealing with navigation techniques for terrestrial navigation. He is currently the head of the TELECOM team of ENAC, that includes research groups on signal processing and navigation, electromagnetics, and data communication networks.